1992

An Observational Streamfunction in the Gulf Stream

Hyun-Sook Kim
University of Rhode Island

D. Randolph Watts
University of Rhode Island, randywatts@uri.edu

Citation/Publisher Attribution

Kim, H-S., & Watts, D. R. (1994). An Observational Streamfunction in the Gulf Stream. . *Phys. Oceanogr., 24*(12), 2639-2657. doi: 10.1175/1520-0485(1994)0242.0.CO;2
Available at: http://dx.doi.org/10.1175/1520-0485(1994)0242.0.CO;2

An Observational Streamfunction in the Gulf Stream

An Observational Streamfunction in the Gulf Stream

HYUN-SOOK KIM AND D. RANDOLPH WATTS

University of Rhode Island, Graduate School of Oceanography, Narragansett Bay Campus, Narragansett, Rhode Island

(Manuscript received 21 December 1992, in final form 29 August 1994)

ABSTRACT

Contours of the main thermocline (12°C isotherm depth: Z_{12}) topography objectively generated from Inverted Echo Sounder observations in the Gulf Stream may be treated as a baroclinic, geostrophic streamfunction ψ. As preliminary steps, the authors developed techniques to estimate geostrophic velocity $\mathbf{V}_\psi = \mathbf{k} \times (g^*/f)\nabla Z_{12}$ and geostrophic vorticity $\zeta_\psi = (g^*/f)\nabla^2 Z_{12}$. In doing this the authors also determined a reduced gravity $g^* = 1.53$ cm s^{-2} by least-squares fitting the estimated $\mathbf{V}_\psi$ to observed $\mathbf{V}_{bc}$ velocities (i.e., fine-tuned for the ψ at 400 m relative to 3000 m).

Accuracy of the objective maps of ψ is investigated by comparing $\mathbf{V}_\psi$ against $\mathbf{V}_{bc}$ directly measured from tall current meter moorings and ζ_ψ against vorticity ζ_p separately estimated using a "rigid-stream" velocity section and path curvature. The $\mathbf{V}_\psi$ values, with speeds up to 100 cm s^{-1}, are correlated with $\mathbf{V}_{bc}$ at the 99% confidence level, and the two measurements differ by only 10 cm s^{-1} rms error. Vorticity estimates, ranging between $-0.44f$ and $+0.64f$, also show excellent agreement between ζ_ψ and ζ_p within 0.77×10^{-5} s^{-1} (or $0.09f$) rms difference. This study carefully documents the objective error-estimation techniques for these fields that, because they are derivatives of the measured ψ field, are sensitive to noise. The objective estimates of error in $\mathbf{V}_\psi$ and ζ_ψ agree in each case with the rms differences from observations.

The authors also illustrate the consequent utility of the objective ψ maps by applying quasigeostrophic calculations to diagnose ageostrophic motions V_a in strong events in the Gulf Stream. The authors found V_a/V_ψ to have peak values of 0.2–0.6. Roughly equal contributions to V_a came in events of large curvature or with high temporal rate of change. Vertical stretching $\partial w/\partial z$ at the 400-m level was estimated using the quasigeostrophic vorticity equation, finding downwelling as large as -4 mm s^{-1} downstream of meander crests, and upwelling as large as 3 mm s^{-1} downstream of meander troughs.

1. Introduction

During the Gulf Stream Dynamics Experiment from April 1983 to May 1985, daily maps of the main thermocline depth (typically represented by the depth of 12°C isotherm: Z_{12}) were produced by objective analysis (OA) applied to Inverted Echo Sounder (IES) measurements of acoustic travel time (τ). Several factors have suggested that these maps behave as streamfunction fields. The contours coincide well with the sea surface temperature patterns; current meter vectors directly observed at 400-m depth tend to parallel the Z_{12} contours; and short segments of the trajectory of isopycnal RAFOS floats are observed to flow approximately along the contours of the maps (Watts et al. 1989).

The conceptual basis that IES measurements determine the streamfunction field began with the study by Watts and Rossby (1977), which found a linear relationship between τ and dynamic height anomaly ΔD. They additionally stressed that because variations in sound speed depend primarily upon temperature, the conversion from τ to ΔD depends indirectly upon density being mainly a function of temperature. In the Gulf Stream region where the T–S relationship is well defined, the IES τ measurements can be interpreted as either Z_{12} or ΔD. Therefore, the streamfunction field, which is determined from the dynamic height field (Pond and Pickard 1983), can be represented by the Z_{12} fields.

In this paper we quantitatively test and verify that the IES objective maps can be most directly interpreted as the baroclinic, geostrophic streamfunction ψ, such that $\psi = \psi(Z_{12})$, a functional relationship of Z_{12}. The following formalisms thus apply for velocity,

---

Corresponding author address: Dr. D. Randolph Watts, Graduate School of Oceanography, University of Rhode Island, Narragansett, RI 02822.

$$\mathbf{V}_\psi = \mathbf{k} \times \nabla\psi = \mathbf{k} \times \frac{g^*}{f} \nabla Z_{12}, \qquad (1)$$

and for vertical vorticity component,

$$\zeta_\psi = \nabla^2\psi = \frac{g^*}{f} \nabla^2 Z_{12}, \qquad (2)$$

where f is the Coriolis parameter, g^* a reduced gravity, and $\mathbf{k}$ a unit vector pointing vertically upward. By proper specification of g^*, this streamfunction applies in the Gulf Stream to a horizon in the upper water column, which for this study is taken to be 400 m deep. This work has the goal of verifying the fields of $\mathbf{V}_\psi$ and ζ_ψ, provided as derivatives of our ψ fields.

Calculating $\mathbf{V}_\psi$ and ζ_ψ from data requires first- and second-order differentiation of our mapped Z_{12} fields—a process which tends to accentuate measurement noise. The prospects might therefore appear more unlikely for investigating quasigeostrophic dynamics from measurements. Nevertheless, following an essential and thorough analysis of error, we show that from measured spatial and temporal changes of the velocity and vorticity, we can demonstrate examples of ageostrophic current and vertical stretching during strong events (such as large amplitude meanders and ring–stream interactions) in the Gulf Stream.

The key concept is that errors in the differentiated quantities depend not only upon the spacing of the input IES Z_{12} measurements but also upon the correlation properties of the output ψ fields imposed by the OA mapping. Evaluations of the derivatives are made using centered finite differences. Hence, there are two types of error considered. One, named "numerical error" ($\mathcal{N}$), is the truncation error owing to replacement of the continuous derivative by a discrete form. The other, named "measurement and statistical error" (σ), is the uncertainty that arises because the gridded estimates of ψ have error, and it may be statistically correlated between the grid points due to, for instance, filtering and the OA procedure itself. Both uncertainties depend upon the grid spacing, such that $\mathcal{N}$ grows and σ decays with increasing spacing. We determine the best grid spacing that minimizes the total uncertainty.

The measurements and mapping the streamfunction fields will next be described, including the determination of an optimum value of reduced gravity g^* (specifically for the 400-m horizon relative to 3000 m). Section 3 documents objective error estimations for derivatives of geostrophic velocity $\mathbf{V}_\psi$ and vorticity ζ_ψ. Verifications of the $\mathbf{V}_\psi$ and ζ_ψ are presented in sections 4 and 5. These two sections illustrate how the results may be applied to subsequent investigation of quasigeostrophic dynamics. In section 6, we analyze contributions to ageostrophic motion in the Gulf Stream, particularly during strong events. Last, we make estimates of each term in the quasigeostrophic vorticity equation and examine the relationship of downward and upward vertical motion to meandering motion.

Overall, this study is intended to lay the foundation for later studies of Gulf Stream dynamics. They include the development and propagation of meanders, using an "equivalent barotropic" model (Kim 1994), working with the quasigeostrophic tendency equation, and diagnosing vertical stretching.

2. Measurements and mapping the streamfunction ψ fields

As part of the Gulf Stream Dynamics Experiment, IES measurements were made at 21 sites approximately 200–600 km downstream of Cape Hatteras during the period April 1983–May 1985. The array of instruments consisted of six cross-stream lines normal to the historical mean path of the Gulf Stream, with spacings of about 60 km cross stream and 65 km downstream. Figure 1 shows the locations of moored IESs by solid squares and circles. Additionally, the circles labeled B2, B3, C1, C2, and C3 indicate tall moorings with current meters (CMs) deployed from 1984 to 1985. Each mooring had current meters at four nominal depths of 400 m, 900 m, 1900 m, and 3000 m below the sea surface. All of the time series of IES and CM measurements have been 40-hour low-pass filtered and subsampled at six-hour intervals as described in technical reports by Tracey et al. (1985), Tracey and Watts (1986), and Bane et al. (1989).

The topography of Z_{12} is objectively mapped daily from the set of IES Z_{12} records by a Gauss–Markoff method adapted for mapping the thermal front region of the Gulf Stream (Watts et al. 1989). The Z_{12} OA maps may be produced on various output grid spacings to have later flexibility for finite differencing of $\mathbf{V}_\psi$ and ζ_ψ. In the following discussion (section 3), we show that different OA-output grid spacings are optimal, depending on which finite-difference quantity is being estimated, $\mathbf{V}_\psi$ or ζ_ψ.

Because IESs were located on each of the CM mooring sites, the gradients ∇Z_{12} could be well estimated at sites B2, C2, and C3 (but less well at end sites B3 and C1). Sites B2 and C2 had complete 24-month velocity records at both 400 and 3000 m, but unfortunately C3 had no good data at 400 m. Consequently, B2 and C2 were chosen as the comparison sites for optimizing the constant g^* (discussed below) as well as for verifying the time series $\mathbf{V}_\psi$.

An example of a 20-km gridded Z_{12} map (13 July 1984) is shown by the inset in Fig. 1. The arrows in this figure show the currents on this date at sites B2 and C2, measured by the CMs at depth 400 m. The shaded areas in the figure indicate features that are less reliable due to higher mapping error; the error is in general small near the IES sites and increases with distance.

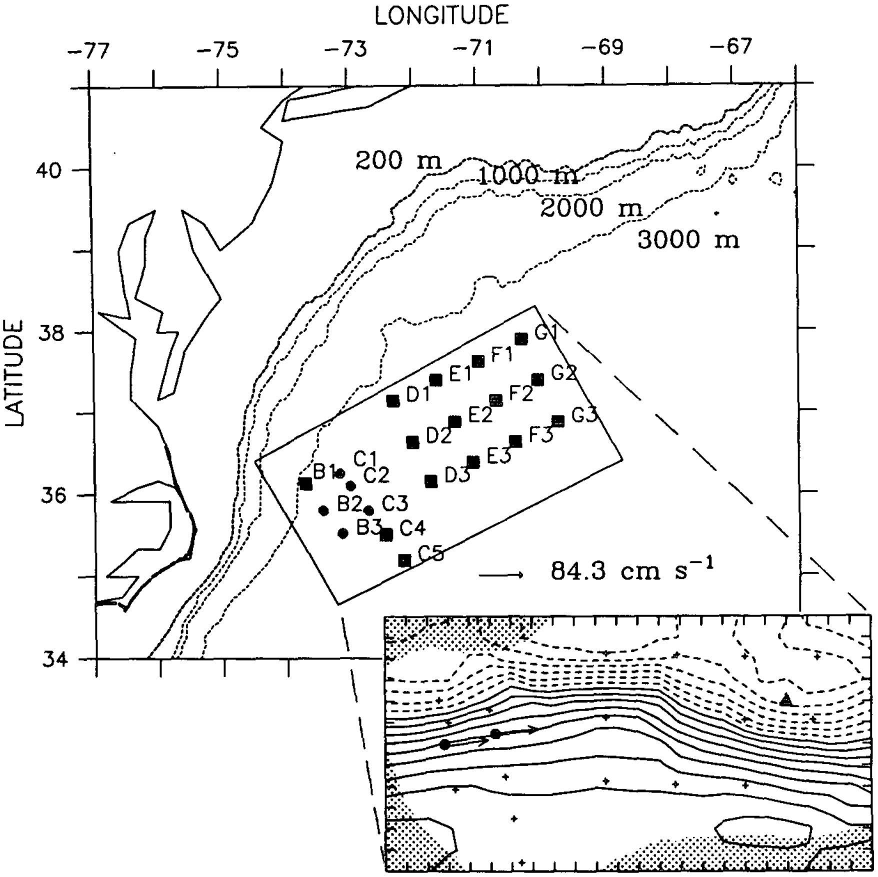

FIG. 1. Tall current meter mooring (●) and IES (■ as well as ●) deployment sites in the study area. The rectangular box (240 km × 460 km), oriented along 64°T, represents the region mapped by objective analysis. The inset shows an example of the mapped thermocline topography for 13 July 1984. Solid contours indicate $Z_{12} \geq 400$ m, the contour interval is 50 m, shaded areas have $\geq$35% mapping error, and ▲ designates site S2. Current vectors at 400 m for sites B2 and C2 (●) are also shown for this date.

To estimate path curvature, we interpolated the OA field onto a 4-km grid using a cubic B spline (Inoue 1986). We chose the minimal smoothing that did not introduce features at shorter spatial scales than our original OA grid (details are presented in Kim 1991).

We determined the best value of reduced gravity g^* using Eq. (1) and the observations of currents and ∇Z_{12} as follows. We minimized the norm of the vector difference $\mathbf{V}_\psi - \mathbf{V}_{bc}$ (where $\mathbf{V}_{bc} = \mathbf{V}_{400} - \mathbf{V}_{3000}$, the observed baroclinic component at 400 m relative to 3000 m) to find

$$g^* = f\frac{\sum_i |\mathbf{V}_{bc}|_i |\nabla Z_{12}|_i \cos\theta_i}{\sum_i |\nabla Z_{12}|_i^2}, \qquad (3)$$

where the sum is over a time series of measurements i; $|\mathbf{V}_{bc}|_i$ and $|\nabla Z_{12}|_i$ are the magnitudes of two vector elements, and θ_i is the angle between them. To determine $\mathbf{V}_\psi$ with minimum estimated uncertainty, we chose an OA grid spacing of 24 km, as explained in section 3, to calculate the gradient ∇Z_{12}. The sum in Eq. (3) excluded large curvature and rapidly evolving events in order to find a value of g^* most approximate for a geostrophic streamfunction. This procedure gave $g^* = 1.53 \pm 0.06$ cm s^{-2}, appropriate for the current at 400 m relative to 3000 m.

3. Error estimates for ψ derivatives, V_ψ and ζ_ψ

In this study, all derivatives of the ψ field ($\mathbf{V}_\psi$ and ζ_ψ) are calculated using centered finite differences.[1] We

---

[1] An alternative approach to calculate the ψ derivatives, such as $\mathbf{V}_\psi$ and ζ_ψ, would be via objective analysis using the techniques of Bretherton et al. (1976) and Qian and Watts (1992). In that case error estimate fields could be provided directly by the objective analysis.

now examine, respectively, the gradient ∇ and the Laplacian ∇^2 operators, which are each subject to two types of error, "numerical error" and "measurement and statistical error," as briefly mentioned in the introduction. We summarize both error sources here. This guides our choice of the best grid spacing for each differential operator.

a. Error estimates and minimization for geostrophic velocities

On a uniform grid of points separated by distance Δ, the centered difference formula of velocity $\mathbf{V}_\psi = -\psi_y\mathbf{i} + \psi_x\mathbf{j}$ expressed in x, y components at point (i, j) is

$$\mathbf{V}_\psi = -\left\{\frac{\psi(i, j+\Delta) - \psi(i, j-\Delta)}{2\Delta} - \frac{\Delta^2}{6}\psi_{yyy}(i, \eta)\right\}\mathbf{i} + \left\{\frac{\psi(i+\Delta, j) - \psi(i-\Delta, j)}{2\Delta} - \frac{\Delta^2}{6}\psi_{xxx}(\xi, j)\right\}\mathbf{j}, \quad (4)$$

where ψ_{xxx} and ψ_{yyy} represent the maximum values of the third-order derivatives of ψ with respect to x and y for the ranges $i - \Delta \leqslant \xi \leqslant i + \Delta$ and $j - \Delta \leqslant \eta \leqslant j + \Delta$. The terms on the rhs, which include ψ_{xxx} and ψ_{yyy}, are the standard numerical truncation errors (generally of unknown sign) that arise from centered finite differencing (Ames 1977). The vector component errors are independent, and the numerical error $\mathscr{N}_{\mathbf{V}_\psi}$ may be expressed as

$$\mathscr{N}_{\mathbf{V}_\psi} = \begin{bmatrix} \dfrac{\Delta^2}{6}\psi_{yyy}(i, \eta) \\ -\dfrac{\Delta^2}{6}\psi_{xxx}(\xi, j) \end{bmatrix}. \quad (5)$$

Quantitative estimates of ψ_{xxx} and ψ_{yyy} may be obtained by modeling the Z_{12} topography as an analytic function of space and time:

$$Z(x, y, t) = Z_0 + A\tanh\left(\frac{y - y_0(x, t)}{W}\right);$$

$$y_0(x, t) = B\cos\left(\frac{2\pi}{L}x - \frac{2\pi}{T}t\right), \quad (6)$$

where typical values are $Z_0 = 450$ m, $A = 400$ m, $B = 50$ km, $W = 40$ km, $L = 350$ km, and $T = 30$ days. Accounting for the factor $(g^*/f)^{-1} = 5.6$ s km^{-1}, we find maximum values of $|\psi_{xxx}| \sim 2.8 \times 10^{-12}$ cm^{-1} s^{-1} and $|\psi_{yyy}| \sim 5.6 \times 10^{-12}$ cm^{-1} s^{-1}.

The second type of error, measurement and statistical error, propagates through objective mapping of the measurements, abbreviated as "statistical error" σ_{V_ψ}. It may be estimated by an expected value of error variance of each velocity component,

$$\sigma^2_{\mathbf{V}_\psi} = \begin{bmatrix} E[e_{\psi_y}e_{\psi_y}] \\ E[e_{\psi_x}e_{\psi_x}] \end{bmatrix},$$

using $e_{\mathbf{V}_\psi} \equiv \mathbf{V}_\psi - \widehat{\mathbf{V}}_\psi$ and accounting for each vector component, expressed as $e_{\mathbf{V}_\psi} = e_{\psi_y}\mathbf{i} + e_{\psi_x}\mathbf{j}$.

The measurement uncertainty $e_{\psi_x} = -\psi_x - (-\widehat{\psi}_x)$ is expressed as

$$e_{\psi_x} = \frac{1}{2\Delta}[\{\psi(i+\Delta, j) - \hat{\psi}(i+\Delta, j)\} - \{\psi(i-\Delta, j) - \hat{\psi}(i-\Delta, j)\}]$$
$$= \frac{1}{2\Delta}[e(i+\Delta, j) - e(i-\Delta, j)].$$

Expanding the linear operator E on variance of the component $e_{\psi_x}e_{\psi_x}$,

$$E[e_{\psi_x}e_{\psi_x}] = \frac{1}{(2\Delta)^2}\begin{pmatrix} E[e(i+\Delta, j)e(i+\Delta, j)] \\ \quad -E[e(i-\Delta, j)e(i+\Delta, j)] \\ -E[e(i+\Delta, j)e(i-\Delta, j)] \\ \quad +E[e(i-\Delta, j)e(i-\Delta, j)] \end{pmatrix}.$$

It may be rewritten, using the shorthand notation of appendix A, [Eq. (19)] for a single time and assuming symmetry, as

$$E[e_{\psi_x}e_{\psi_x}] = \frac{1}{(2\Delta)^2}[\mathscr{E}(1, 0; 1, 0) - 2\mathscr{E}(-1, 0; 1, 0) + \mathscr{E}(-1, 0; -1, 0)].$$

Using the analogous expression for $E[e_{\psi_y}e_{\psi_y}]$ and combining these expressions, the statistical error σ_{V_ψ} is the root of

$$\sigma^2_{\mathbf{V}_\psi} = \frac{1}{(2\Delta)^2}\begin{bmatrix} \mathscr{E}(1, 0; 1, 0) - 2\mathscr{E}(-1, 0; 1, 0) \\ \quad + \mathscr{E}(-1, 0; -1, 0) \\ \mathscr{E}(0, 1; 0, 1) - 2\mathscr{E}(0, -1; 0, 1) \\ \quad + \mathscr{E}(0, -1; 0, -1) \end{bmatrix}. \quad (7)$$

The combined numerical and statistical error in our V_ψ estimate is

$$\delta(V_\psi) = \{|\mathscr{N}_{\mathbf{V}_\psi}|^2 + |\sigma^2_{\mathbf{V}_\psi}|\}^{1/2}.$$

These two error contributions may be seen from Eqs. (5) and (7) to be oppositely affected by the grid spacing Δ.

Increasing Δ increases the numerical error $|\mathscr{N}_{\mathbf{V}_\psi}|$ and decreases the statistical error $|\sigma^2_{\mathbf{V}_\psi}|^{1/2}$. We have estimated $|\mathscr{N}_{\mathbf{V}_\psi}|$ and $|\sigma^2_{\mathbf{V}_\psi}|^{1/2}$ as a function of the grid spacing Δ in Fig. 2 for values of Δ from 12 to 40 km. The total error (solid line) may be minimized

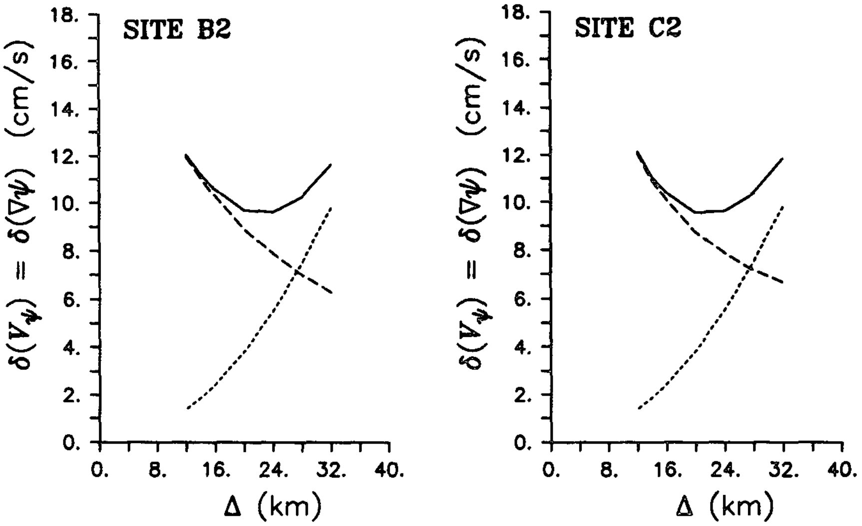

FIG. 2. Numerical error $|\mathcal{N}_{V_\psi}|$ (dotted), statistical error $|\sigma^2_{V_\psi}|^{1/2}$ (dashed), and the combined error (solid) in estimates $V_\psi = |\mathbf{k} \times \nabla\psi|$.

by the appropriate selection of Δ. When $\Delta > 28$ km, the combined error grows due to $|\mathcal{N}_{V_\psi}|$ domination, and where $\Delta < 16$ km, it grows due to $|\sigma^2_{V_\psi}|^{1/2}$ domination. We chose $\Delta = 24$ km as the optimal grid spacing, because it is in the range of minimum estimated uncertainty for both sites of B2 and C2, with corresponding uncertainty in velocity $\delta(V_\psi) = 9.6$ cm s^{-1}.

b. Error estimates and minimization for geostrophic vorticities

The difference approximation for the Laplacian $\nabla^2\psi$ is a sum of the second-order centered difference estimates in x and y:

$$\nabla^2\psi \approx \frac{\psi(i+\Delta, j) - 2\psi(i,j) + \psi(i-\Delta, j)}{\Delta^2} + \frac{\psi(i, j+\Delta) - 2\psi(i,j) + \psi(i, j-\Delta)}{\Delta^2}. \quad (8)$$

The standard numerical truncation error for $\zeta_\psi = \nabla^2\psi$, $\mathcal{N}_{\zeta_\psi}$, is summed for each independent component as

$$\mathcal{N}_{\zeta_\psi} = \left\{\left(-\frac{\Delta^2}{12}\psi_{xxxx}(\xi, j)\right)^2 + \left(-\frac{\Delta^2}{12}\psi_{yyyy}(i, \eta)\right)^2\right\}^{1/2}. \quad (9)$$

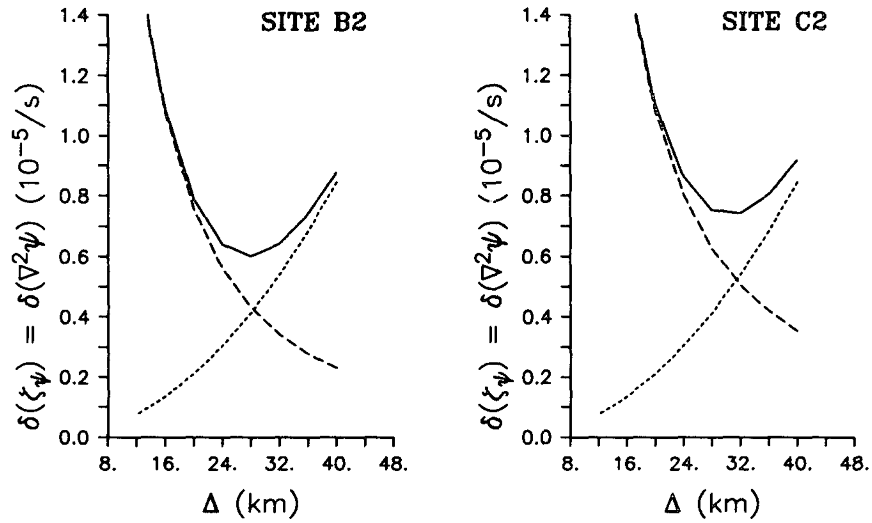

FIG. 3. Numerical error $\mathcal{N}_\zeta$ (dotted), statistical error σ_ζ (dashed), and the combined error (solid) in estimates $\zeta_\psi = \nabla^2\psi$.

The maximum values of ψ_{xxxx} and ψ_{yyyy} may be estimated by using the idealized Z_{12} model given by Eq. (6) with $g^*/f = 0.18$ km s^{-1}. We obtained $|\psi_{xxxx}| \sim 1.3 \times 10^{-18}$ cm^{-2} s^{-1} and $|\psi_{yyyy}| \sim 2.9 \times 10^{-18}$ cm^{-2} s^{-1}.

To solve for the statistical error σ_ζ, we again start with its variance $\sigma^2_{\zeta_\psi} = E[e_{\zeta_\psi} e_{\zeta_\psi}]$, where $e_{\zeta_\psi} = e_{\psi_{xx}} + e_{\psi_{yy}}$. Expanding, we find

$$\sigma^2_{\zeta_\psi} = E[e_{\psi_{xx}} e_{\psi_{xx}}] + 2E[e_{\psi_{xx}} e_{\psi_{yy}}] + E[e_{\psi_{yy}} e_{\psi_{yy}}]. \quad (10)$$

The component error $e_{\psi_{xx}}$ is calculated using the error definition of the estimates in Eq. (8) as

$$e_{\psi_{xx}} = \frac{1}{\Delta^2}[e(i+\Delta, j) - 2e(i, j) + e(i-\Delta, j)]. \quad (11)$$

The error covariances in Eq. (10) are computed by cross-correlations between $e_{\psi_{xx}}$ of Eq. (11) and $e_{\psi_{yy}}$ obtained in a similar way. For instance, using the shorthand of Eq. (19) for a linear expansion of the E operator on the variance $e_{\psi_{xx}} e_{\psi_{xx}}$,

$$E[e_{\psi_{xx}} e_{\psi_{xx}}] = \frac{1}{\Delta^4}\begin{pmatrix} \mathcal{E}(1, 0; 1, 0) + 4\mathcal{E}(0, 0; 0, 0) + \mathcal{E}(-1, 0; -1, 0) \\ -4\mathcal{E}(1, 0; 0, 0) - 4\mathcal{E}(0, 0; -1, 0) + 2\mathcal{E}(1, 0; -1, 0) \end{pmatrix}. \quad (12)$$

Here $E[e_{\psi_{yy}} e_{\psi_{yy}}]$ may be obtained analogously by accounting for symmetry: for instance, $\mathcal{E}(1, 0; 1, 0)$ translates to $\mathcal{E}(0, 1; 0, 1)$. In a similar way,

$$E[e_{\psi_{xx}} e_{\psi_{yy}}] = \frac{1}{\Delta^4}\begin{pmatrix} \mathcal{E}(1, 0; 0, 1) - 2\mathcal{E}(1, 0; 0, 0) + \mathcal{E}(1, 0; 0, -1) \\ -2\mathcal{E}(0, 0; 0, 1) + 4\mathcal{E}(0, 0; 0, 0) - 2\mathcal{E}(0, 0; 0, -1) \\ +\mathcal{E}(-1, 0; 0, 1) - 2\mathcal{E}(-1, 0; 0, 0) + \mathcal{E}(-1, 0; 0, -1) \end{pmatrix}. \quad (13)$$

Following Eq. (10) the statistical error σ_ζ is the root of the sum of Eq. (12), twice Eq. (13), and the shorthand-expression for $E[e_{\psi_{yy}} e_{\psi_{yy}}]$,

$$\sigma^2_{\zeta_\psi} = \frac{1}{\Delta^4}\begin{pmatrix} \mathcal{E}(1, 0; 1, 0) & +\mathcal{E}(-1, 0; -1, 0) & +\mathcal{E}(0, 1; 0, 1) \\ +\mathcal{E}(0, -1; 0, -1) & +16\mathcal{E}(0, 0; 0, 0) & +2\mathcal{E}(1, 0; -1, 0) \\ +2\mathcal{E}(0, 1; 0, -1) & +2\mathcal{E}(1, 0; 0, 1) & +2\mathcal{E}(1, 0; 0, -1) \\ +2\mathcal{E}(-1, 0; 0, 1) & +2\mathcal{E}(-1, 0; 0, -1) & -8\mathcal{E}(1, 0; 0, 0) \\ -8\mathcal{E}(0, 0; 0, 1) & -8\mathcal{E}(-1, 0; 0, 0) & -8\mathcal{E}(0, 0; 0, -1) \end{pmatrix}, \quad (14)$$

in which we have combined terms to account for symmetries, such as $\mathcal{E}(-1, 0; 0, 0) = \mathcal{E}(0, 0; -1, 0)$.

The combined numerical and statistical errors of our finite-differencing estimate ζ_ψ is then

$$\delta(\zeta_\psi) = \{\mathcal{N}^2_{\zeta_\psi} + \sigma^2_{\zeta_\psi}\}^{1/2}. \quad (15)$$

For the latter expression, we recognize that the sum of the $\mathcal{E}$ in Eq. (14) varies weakly with Δ, and the fourth-order derivative maxima in Eq. (9) are constants. Hence, the total error (Fig. 3) again has a minimum between the two regimes, in which statistical error σ_{ζ_ψ} prevails when $\Delta < 24$ km, and numerical error $\mathcal{N}_{\zeta_\psi}$ prevails when $\Delta > 36$ km. We have used $\Delta = 28$ km for computing the Laplacian operator, with corresponding minimum error in vorticity $\delta(\zeta_\psi) = 0.76 \times 10^{-5}$ s^{-1}.

4. Geostrophic velocity

In this section, geostrophic velocity $\mathbf{V}_\psi$ estimates, from the OA maps using Eq. (1) and the method developed in section 3a, are compared to direct measurements of currents. Accounting for baroclinicity, the verification measurements are the shear velocities $\mathbf{V}_{bc}$ between the observed currents at 400-m and 3000-m depths.

Figure 4 shows stick plots of both $\mathbf{V}_\psi$ and $\mathbf{V}_{bc}$ at B2 and C2. In general, the estimated velocity $\mathbf{V}_\psi$ agrees well with the observed $\mathbf{V}_{bc}$ in both magnitude and direction. The northeastward flow of the Gulf Stream (typically 50–100 cm s^{-1}) is evident throughout most of these records, and in addition two major cyclonic disturbances, caused by interactions of cold rings with the Gulf Stream, are equally captured by both $\mathbf{V}_\psi$ and $\mathbf{V}_{bc}$.

The magnitude V_ψ and V_{bc} and the u(eastward) and v(northward) components of velocity $\mathbf{V}_\psi$ and $\mathbf{V}_{bc}$ for B2 are illustrated in Fig. 5 along with their error bars. There is striking agreement between the u components, which differ by only 10 cm s^{-1} rms compared to a signal ranging from −50 to +80 cm s^{-1}. The agreement for the v component is not as good, differing by 12 cm s^{-1} rms compared to the range from −20 to +70 cm s^{-1}. The $u'_\psi = -\partial\psi/\partial y$ estimates from the OA maps are more accurate than the $v'_\psi = \partial\psi/\partial x$ estimates, because the IES sites are more closely spaced meridionally (y) than zonally (x) and because no IESs are located upstream of site B2 to help estimate $\partial\psi/\partial x$. The objective error covariances ($\mathcal{E}$'s from section 3a) reflect this, as indicated by the error bars for (u_ψ, v_ψ) shown in Fig. 5.

We summarize the velocity comparisons in Table 1, by listing the means, rms values, rms differences,

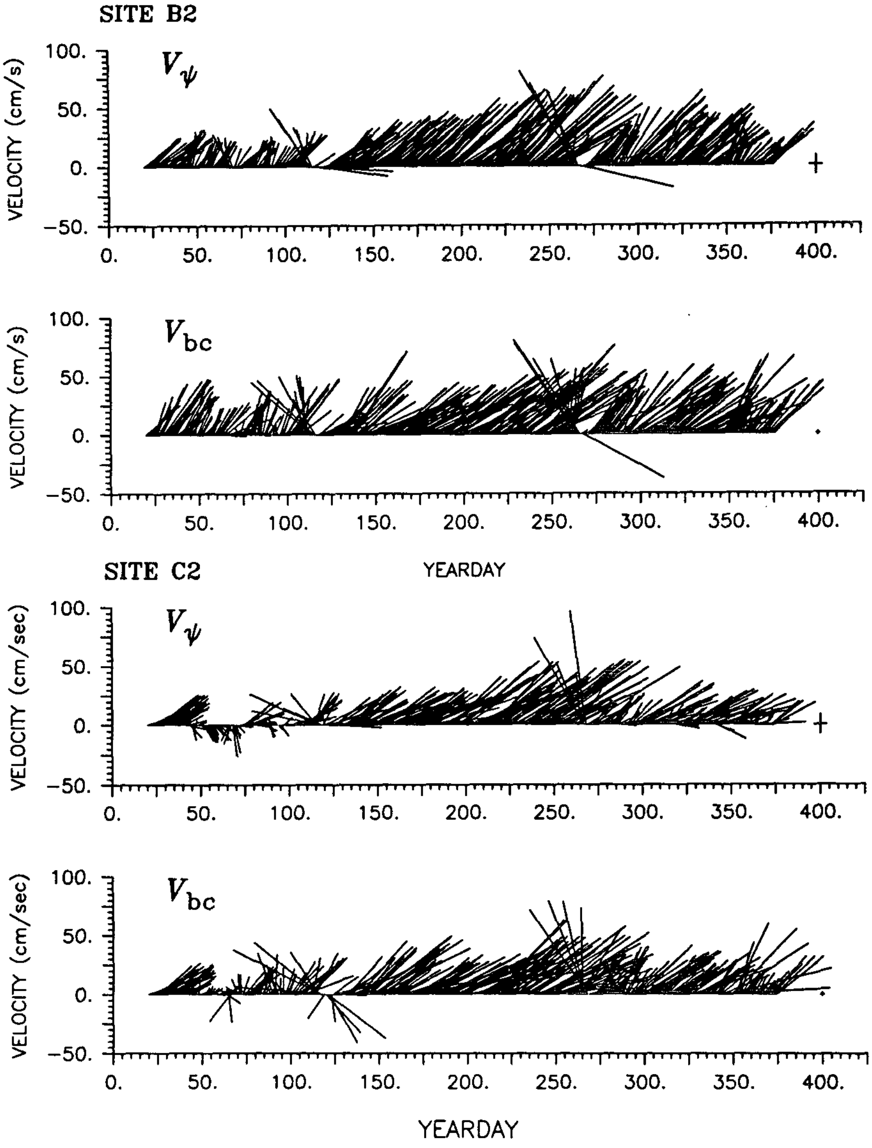

FIG. 4. Stick plots for estimated current $\mathbf{V}_\psi$ and observed current $\mathbf{V}_{bc}$ at sites B2 and C2. The x axis is eastward, y axis is northward, and the cross bars at the right indicate their uncertainties, ±1 std dev.

and correlation coefficients of the several variables. These results quantitatively confirm the visual similarities seen in Figs. 4 and 5. However, the correlation r of the v components at C2 has a slightly lower value because there is a larger downstream gap between IES measurement sites. The correlations of the other two variables are high: $r = 0.98$.

The estimated uncertainties in $\mathbf{V}_\psi$ (in section 3) and in $\mathbf{V}_{bc}$ predict well the observed rms differences. Hence, we attribute the source of most of these differences to noise in $\mathbf{V}_\psi$ instead of to ageostrophic components of the velocities (see also section 6a).

To illustrate the power and utility of this methodology, beyond just estimating the velocity at a point, the baroclinic velocity $\mathbf{V}_\psi(x, y, t)$ may be calculated as a time series field of $\mathbf{V}_\psi(x, y)$ along with error estimates at all points in the field. A three-day sequence of streamfunction and the corresponding velocity $\mathbf{V}_\psi$ maps is illustrated in Fig. 6. During the period, yeardays 114 to 116, a cold ring interacted with the Gulf Stream just southwest of our study area and then propagated into the region. The predicted error for the velocity magnitude is less than 12 cm s^{-1} for V_ψ and less than 8–10 cm s^{-1} for u_ψ and v_ψ over the whole field, ex-

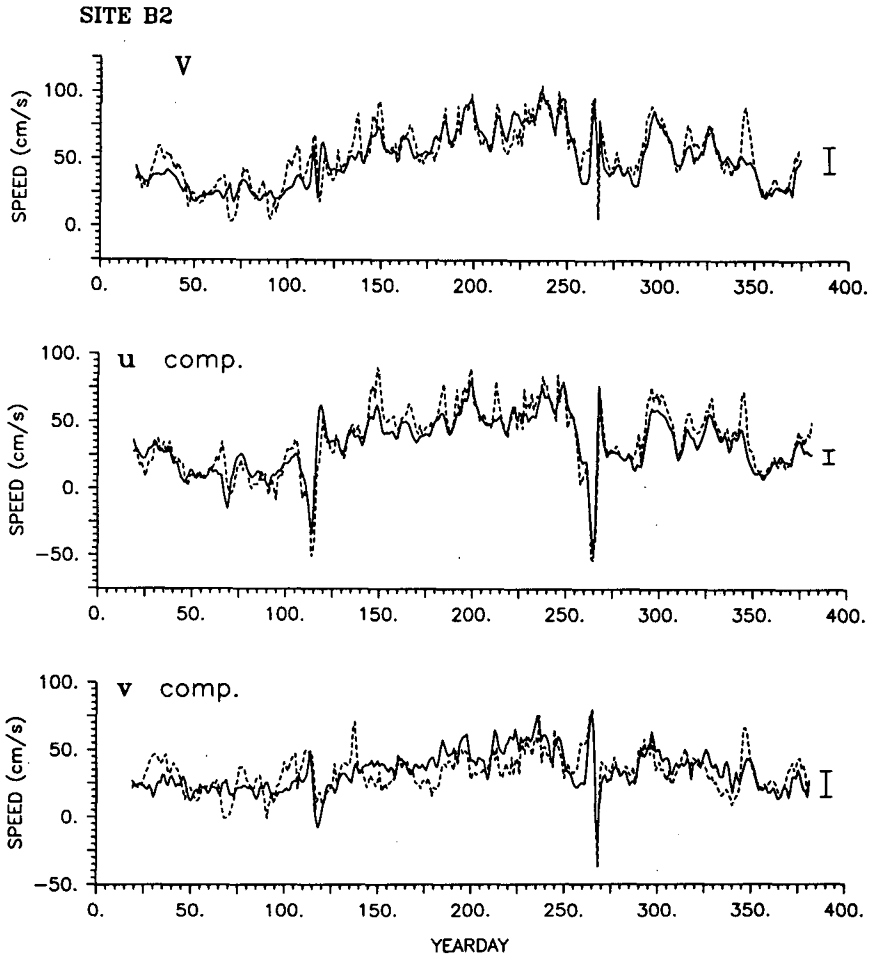

FIG. 5. The magnitudes and u (east) and v (north) components of velocity $\mathbf{V}_\psi$ and $\mathbf{V}_{bc}$ at site B2. In each panel, a solid line indicates the geostrophic current and a dashed line is the observed current. The bars at the right are the predicted uncertainties for the estimated velocity, ±1 std dev limits.

TABLE 1. Velocity comparisons at site B2 and C2: units are cm s^{-1} except for the dimensionless correlation coefficient r.

	u component			v component			Speed		
	u_{bc}		u_ψ	v_{bc}		v_ψ	V_{bc}		V_ψ
					Site B2				
Mean	36.7		33.8	33.6		34.1	53.2		50.1
rms	24.6		20.5	14.0		14.5	21.2		20.5
rms difference		9.8			12.3			8.0	
correlation r		0.98			0.94			0.98	
					Site C2				
Mean	33.7		33.1	24.3		18.6	45.9		41.3
rms	25.4		23.3	15.0		16.5	22.0		23.4
rms difference		8.6			12.4			9.3	
correlation r		0.98			0.87			0.98	
Uncertainty estimate	±1.5		±5.1	±1.5		±8.1	±2.0		±9.6

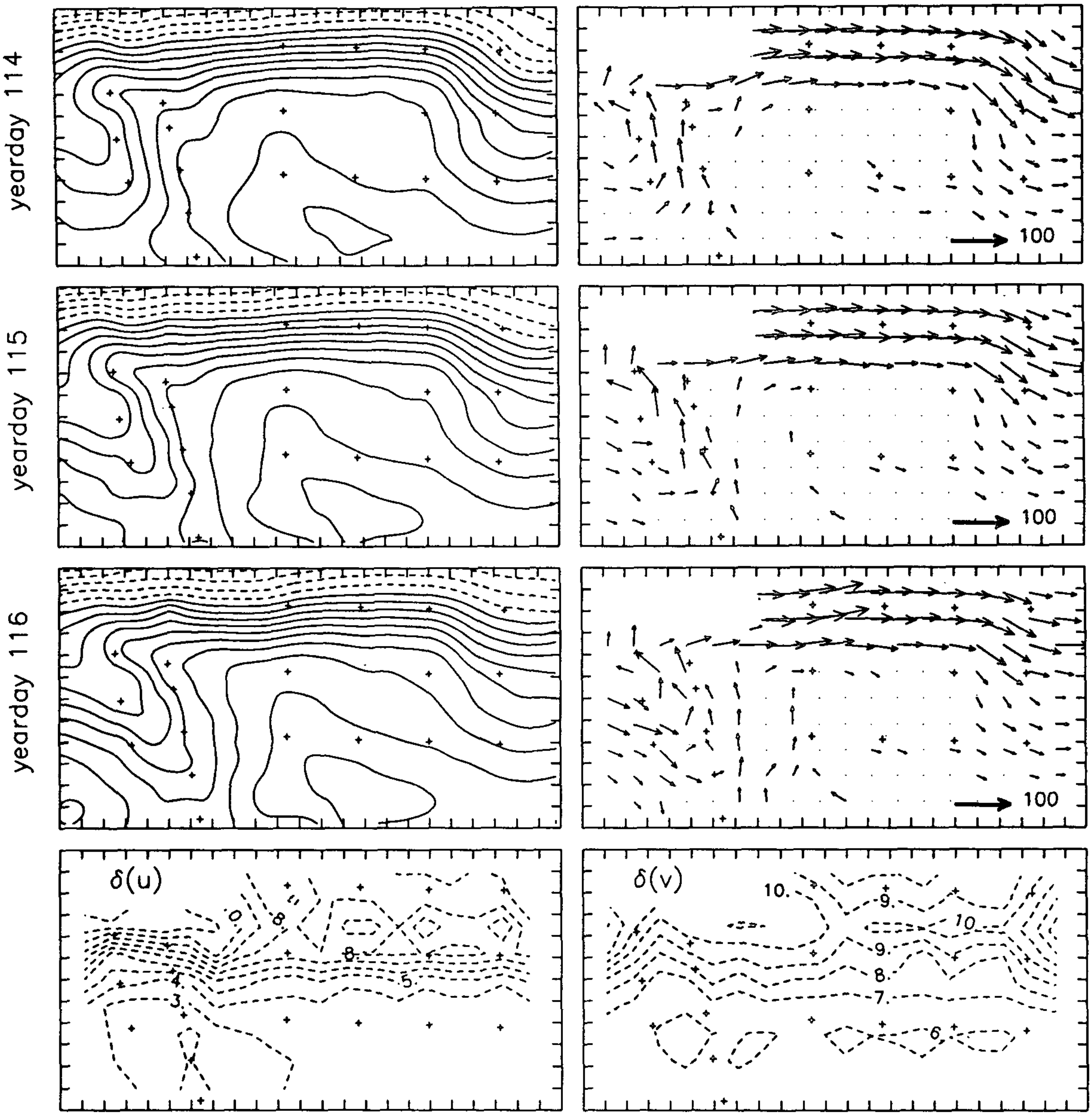

FIG. 6. Three-day sequence of streamfunction ψ (left panels) and velocity $\mathbf{V}_\psi$ (right panels) maps for yeardays 114–116. The bold arrow on $\mathbf{V}_\psi$ maps indicates a velocity of 100 cm s^{-1}. Bottom panels show predicted uncertainty contours of $\delta(u)$ (left) and $\delta(v)$ (right) for the estimated $\mathbf{V}_\psi$. The blanked areas (northwest corners) represent no IES measurements.

cluding the northwest corner (blanked) where there were no IES measurements.

5. Geostrophic vorticity

Geostrophic vorticity ζ_ψ of Eq. (2) may be determined from the Laplacian of the streamfunction field. The methodologies for the ζ_ψ estimates, for objective estimates of uncertainty, and for selecting the best grid spacing are developed in section 3b. In this section, we compare ζ_ψ with a separate determination of relative vorticity ζ_p.

For the second approach, we employ a "rigid stream" assumption that the cross-stream velocity profile does not vary with alongstream distance or time and that the profile simply shifts laterally as the current meanders. This assumption has been found to be a reasonable approximation both by Halkin and Rossby (1985), from observations near 73°W, and by Johns et al. (1994), from observations near 68°W. Under this assumption, we first reexpress relative vorticity in stream coordinates and rearrange

$$\frac{\partial V}{\partial n} = \zeta - \kappa V, \qquad (16)$$

where ζ denotes relative vorticity, κ curvature, κV curvature vorticity, and $\partial V/\partial n$ lateral shear vorticity with the n axis pointing to the right facing downstream.

The mean "stream coordinates" velocity section has been determined from a set of absolute velocity measurements by the Pegasus profiler on the transect at 73°W. For each of 16 cruises during September 1980 to May 1983, the section was transformed into stream coordinates, and these were averaged to construct the mean section (Halkin and Rossby 1985). For consistency with our other analyses, we have computed the baroclinic component (at depth 400 m relative to 3000 m) of the mean alongstream velocity, and we have smoothed the section using a cubic B-spline interpolation. The resulting velocity profile $V(n)$ is shown in Fig. 7a, together with the shear profile $\partial V(n)/\partial n$ in Fig. 7b.

We next use the following method to estimate all the components of Eq. (16) at a given date and location. First, determine the shortest relative normal distance n between that site and the contour of Z_{12} at 400 m on the OA map, which is the $n = 0$ path. Then, infer the lateral shear vorticity $\partial V(n)/\partial n$ from Fig. 7b. Curvature vorticity κV is computed with the estimates of the speed V_ψ and the path curvature κ, obtained by least-squares fitting a circle to ψ (Kim 1991) at the site. Relative vorticity ζ_p is obtained using $\partial V(n)/\partial n$ and κV according to Eq. (16).

We compare the two methods of estimating the vorticity components at site S2, (see the inset in Fig. 1) where the surrounding IES measurements sites ensured that the mapped ψ field would be well resolved. Each of the vorticity constituents at S2 is shown in time series in Fig. 8, where the estimates from the rigid-stream method are indicated by dashed lines. The solid line in Fig. 8c is shear vorticity obtained from ζ_ψ and κV_ψ using Eq. (16). The total uncertainty for the shear vorticity $\partial V/\partial n$ is 0.81×10^{-5} s^{-1}, which is computed as the square root of the sum of the squares of the error $\delta(\zeta_\psi) = 0.76 \times 10^{-5}$ s^{-1} (section 3) and $\delta(\kappa V) = 0.28 \times 10^{-5}$ s^{-1}. The rms value of both estimates of $\partial V/\partial n$ are of the same order, 1.34×10^{-5} s^{-1} ($0.16f$). The rms difference between the two estimates is 0.77×10^{-5} s^{-1} ($0.09f$). The ζ_ψ estimates, ranging from $-0.44f$ to $+0.64f$, agree with ζ_p within the estimated uncertainty.

Therefore, we take this comparison to establish the agreement between ζ_p and ζ_ψ, the rigid-stream model and the $\nabla^2\psi$ methods. The agreement confirms that (i) our calculation of ζ_ψ from $\nabla^2\psi$ indicates the true relative vorticity very well, and (ii) our method to estimate its uncertainty is also accurate.

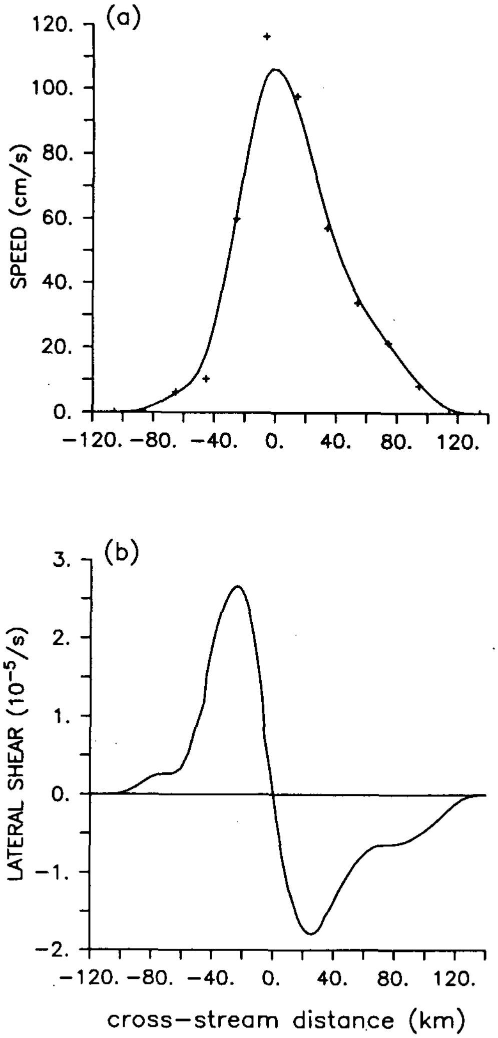

FIG. 7. Pegasus mean alongstream velocity profiles $V(n) = V_{400} - V_{3000}$ in stream coordinates: (a) cross-stream velocity smoothed by a cubic B-spline basis and (b) cross-stream lateral shear. The origin $n = 0$ is set to be the location where the 12°C isotherm crosses a depth of 400 m.

6. Estimation of ageostrophic motion and vertical stretching

Motions associated with strong events, such as the ring–stream interactions seen in Fig. 4, may not be in geostrophic balance because centripetal acceleration and/or tangential acceleration may be strong enough to cause measurable departures from the balance (e.g., Johns et al. 1989). Moreover, horizontal divergence and vertical stretching are associated with these ageostrophic departures.

Based upon our successful velocity field $\mathbf{V}_\psi$ and vorticity field ζ_ψ calculations, we may estimate ageostrophic velocity $\mathbf{V}_a$ quasigeostrophically (Bluestein 1992) using

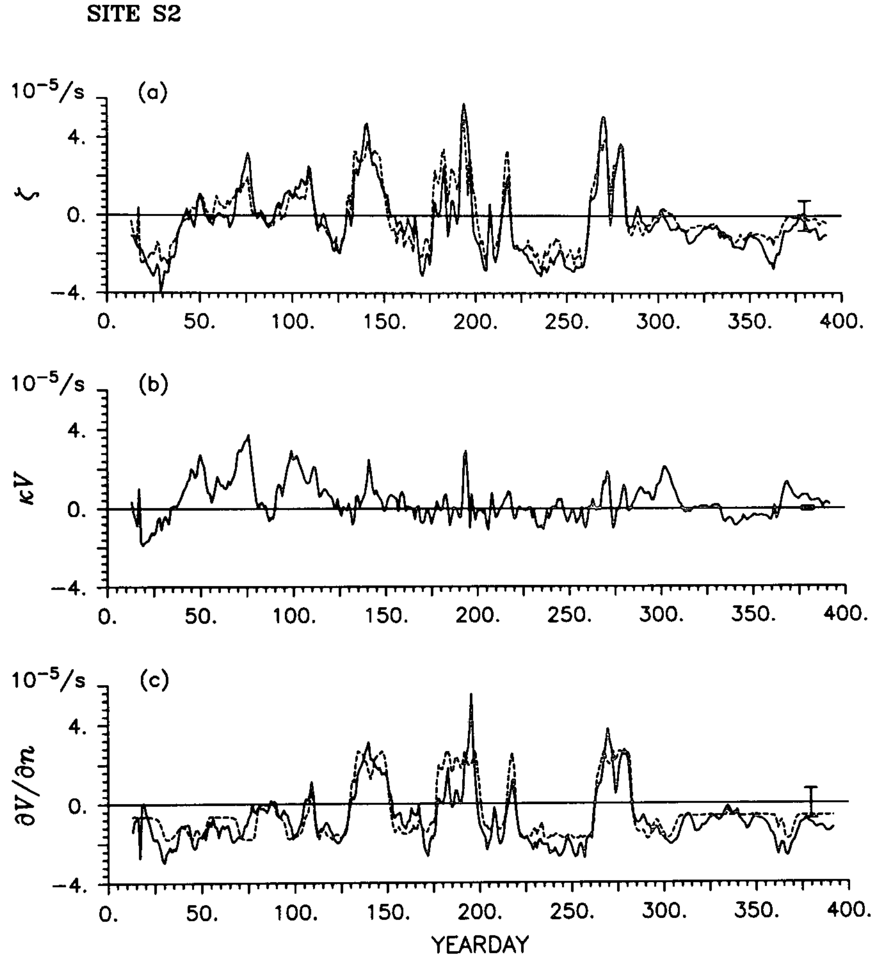

FIG. 8. Vorticity constituents at site S2: (a) relative vorticity ζ: $\zeta_\psi = \nabla^2\psi$ (solid) and $\zeta_p = \kappa V + \partial V/\partial n$ (dashed), (b) curvature vorticity κV, and (c) shear vorticity $\partial V/\partial n$: $\zeta_\psi - \kappa V$ (solid) and the rigid stream estimate from Pegasus data (dashed). The bars at the right on each plot indicate ±1 std dev error.

$$\mathbf{V}_a = \frac{1}{f}\mathbf{k}\times\frac{D_h\mathbf{V}_h}{Dt} = V_{an}\mathbf{n} + V_{at}\mathbf{t}$$

$$\equiv \frac{1}{f}\frac{D_hV_h}{Dt}\mathbf{n} - \frac{1}{f}\kappa V_h^2\mathbf{t}, \qquad (17)$$

where $V_h = V_\psi + V_{3000}$, and $D_h/Dt \equiv \partial/\partial t + \mathbf{V}_h\cdot\nabla$. This is expressed in natural coordinates with unit vectors **t** and **n**, oriented, respectively, parallel and normal to the flow. Similarly, vertical stretching $\partial w/\partial z$ in an incompressible fluid may be determined using the quasigeostrophic vorticity equation (Holton 1979; Bluestein 1992)

$$f\frac{\partial w}{\partial z} = \frac{\partial \zeta}{\partial t} + \mathbf{V}_h\cdot\nabla(\zeta + f), \qquad (18)$$

where $\zeta = \zeta_\psi + \zeta_{3000}$. These estimates are much less subject to measurement or computation noise than the direct subtraction of the geostrophic velocity from the horizontal velocity (Kim 1991) and direct calculation of horizontal divergence (e.g., Bryden and Fofonoff 1977). In both cases, this is because the right-hand sides of Eqs. (17) and (18) deal entirely with terms of $O(\mathrm{Ro}^1)$ (Rossby number Ro), neglecting terms of $O(\mathrm{Ro}^2)$, rather than attempting to directly calculate residuals of differences between $O(\mathrm{Ro}^0)$ quantities in the momentum and continuity equations, respectively.

Our purpose in this section is simply to demonstrate the feasibility of performing these quasigeostrophic calculations with sufficient accuracy to be applied to strong events in the Gulf Stream. We illustrate ageostrophic motion at sites B2 and C2 (section 6a), and vertical stretching at site S2 (section 6b). In addition, the vertical motion will be briefly related to meandering motion of the Gulf Stream.

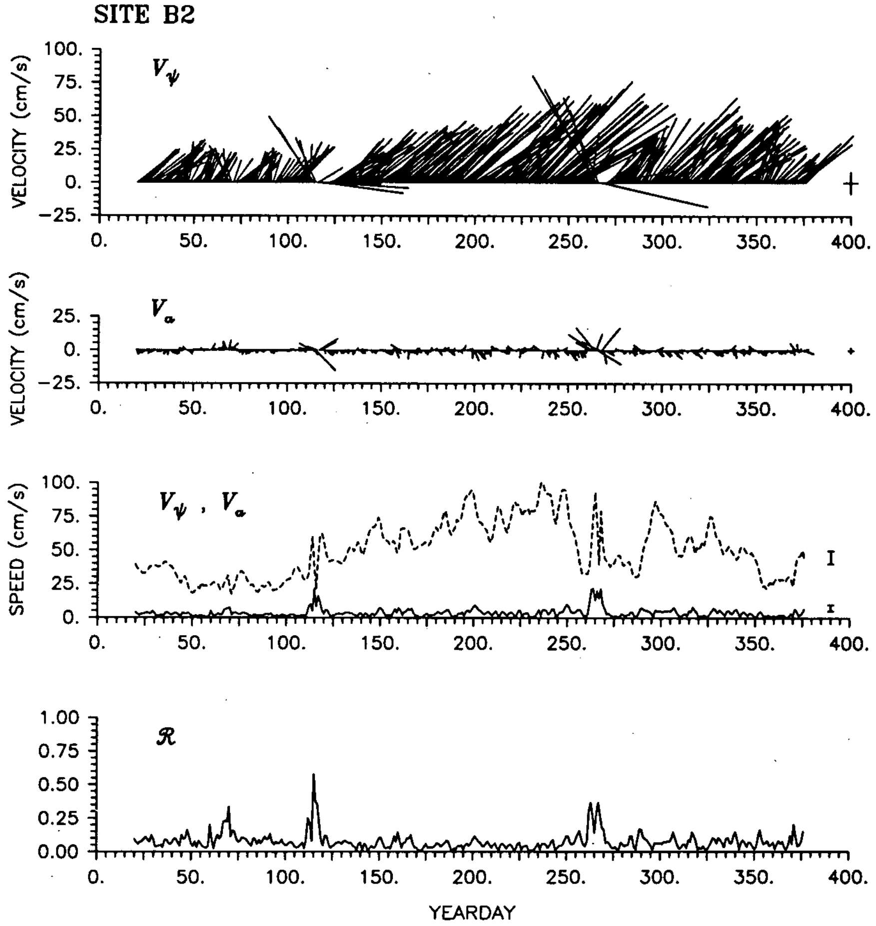

FIG. 9. Daily geostrophic and ageostrophic current vectors, $\mathbf{V}_\psi$ (top) and $\mathbf{V}_a$ (second) at site B2, and magnitudes of V_ψ (dashed) and V_a (solid) are shown in the third panel. The last panel represents a time series of departure ratio $\mathcal{R} = V_a/V_\psi$. The cross bars and vertical bars indicate their uncertainties (±1 std dev). The error bars on $\mathbf{V}_a$ are approximately 2–3 cm s^{-1} in each component.

a. Ageostrophic motion

The ageostrophic velocities $\mathbf{V}_a$ at sites B2 and C2 are calculated using Eq. (17) with our $\mathbf{V}_\psi$ measurements (neglecting $\mathbf{V}_{3000}$), and the associated error $\delta(V_a)$ is documented in appendix B. The uncertainty introduced in $\mathbf{V}_a$ by having neglected $\mathbf{V}_{3000}$ in Eq. (17) is dominated by the advection term $\mathbf{V}_\psi \cdot \nabla \mathbf{V}_{3000}$, which is approximately 20% of the leading terms constituting $\mathbf{V}_a$. This error is no larger than the noise level, $\delta(V_a) = 2$–3 cm s^{-1}, estimated in appendix B. Accordingly, the following investigation is based on $\mathbf{V}_a$ estimates using only the baroclinic $\mathbf{V}_\psi$.

The $\mathbf{V}_a$ vectors at B2 are shown in Fig. 9 with geostrophic velocity $\mathbf{V}_\psi$ at the same site. While many of the $\mathbf{V}_a$ estimates are near the noise level indicated by the small cross at the right (2–3 cm s^{-1}), two strong ageostrophic events with peak speeds near 20 cm s^{-1} are clearly detected at yeardays 115 (24 April) and 265 (21 September).

We closely examine the event at yeardays 111–125 (April event). Plotting the velocities and their components at sites B2 and C2 on expanded scales, respectively, in the left and right panels of Fig. 10 reveals that the event consists of three separate departures from geostrophy. At site B2, these peaks occur at yeardays 113, 115, and 117 (see left panel of Fig. 10a). The corresponding evolution of the Gulf Stream path is shown by the sequences of daily Z_{12} maps from yeardays 111–119 in Fig. 11. On days 111–114, the Gulf Stream is perturbed by the coalescence of a cold ring in the region just upstream of our array. As the disturbance propagates into the study area, the thermocline steepens near sites B2 and C2 (Fig. 11), and the geostrophic velocity V_ψ is accelerated. Figure 10a shows V_ψ increasing from 29 to 60 cm s^{-1} between yeardays 111–114. Examination of the components of V_{an} reveals that the advective changes $(1/f)V_\psi(\partial V_\psi/\partial s)$ only weakly oppose the dominant local tendency $(1/f)(\partial V_\psi/\partial t)$. Furthermore, contributions from

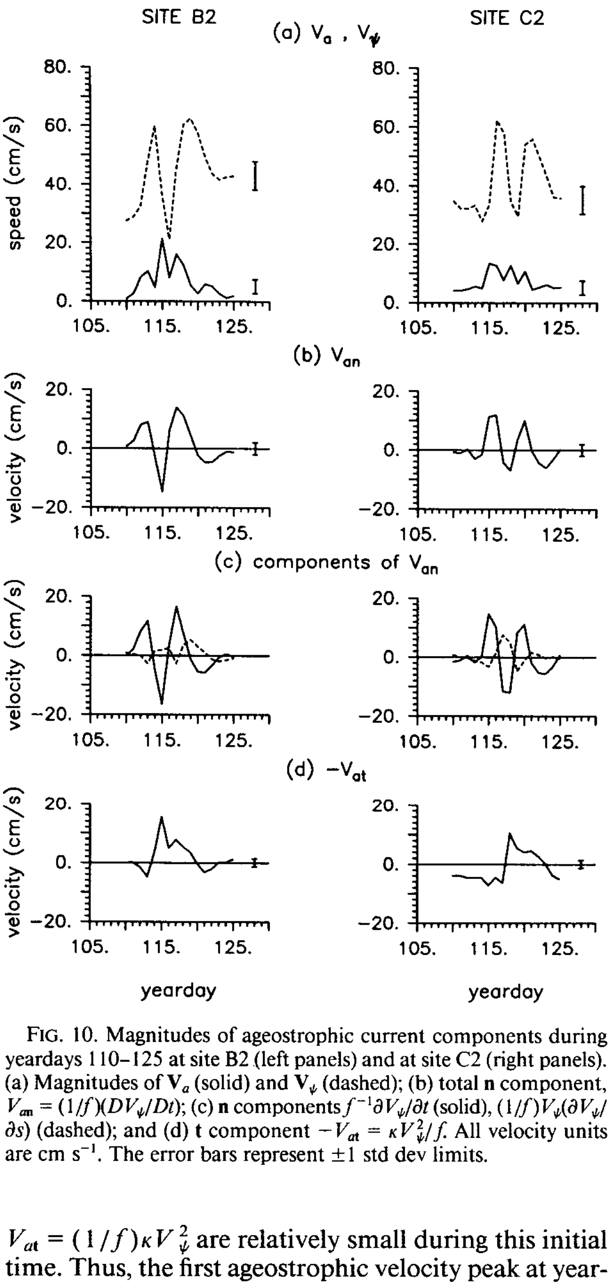

FIG. 10. Magnitudes of ageostrophic current components during yeardays 110–125 at site B2 (left panels) and at site C2 (right panels). (a) Magnitudes of $\mathbf{V}_a$ (solid) and $\mathbf{V}_\psi$ (dashed); (b) total **n** component, $V_{an} = (1/f)(DV_\psi/Dt)$; (c) **n** components $f^{-1}\partial V_\psi/\partial t$ (solid), $(1/f)V_\psi(\partial V_\psi/\partial s)$ (dashed); and (d) **t** component $-V_{at} = \kappa V_\psi^2/f$. All velocity units are cm s^{-1}. The error bars represent ±1 std dev limits.

$V_{at} = (1/f)\kappa V_\psi^2$ are relatively small during this initial time. Thus, the first ageostrophic velocity peak at yearday 113 primarily results from changes in the magnitude of V_ψ. Using $V_\psi = 32$ cm s^{-1} and $V_a = 8$ cm s^{-1}, this peak has a "departure ratio," $\mathcal{R} \equiv V_a/V_\psi$, of 0.25 (Fig. 9). The second peak, however, is caused by centripetal acceleration. During days 115–116, V_ψ decreases (Fig. 10a) as the ring center passes over site B2 (Fig. 11), and we find there is a local maximum of 15.4 cm s^{-1} in V_{at} due to centripetal acceleration. This is accompanied by a local minimum of -14.6 cm s^{-1} in V_{an}. This middle peak has $\mathcal{R} = 0.58$. Finally, after the ring center propagates past site B2 on day 117, V_ψ once again increases sharply. These changes in V_ψ give rise to the third ageostrophic peak, with $\mathcal{R} = 0.35$. The full ageostrophic event ends with a drop in V_ψ caused by the straightening of the Gulf Stream path as the ring is advected farther downstream.

The right panels of Fig. 10 show the same sequence of ageostrophic peaks at site C2 delayed by about 3 days. Similar results were also obtained at both sites for the second event in September (not shown). In each instance, the ageostrophic event was composed of three separate departures. The first and last of these peaks were caused primarily by V_{an} with strong advection and rapid tendency in V_ψ, while the middle peak was dominated by V_{at} due to centripetal acceleration. However, during September when the Gulf Stream path was more highly curved by the coalescing ring, centripetal accelerations contributed more substantially to the ageostrophic peaks (Kim 1991). It was during this event that the largest V_a/V_ψ ratio ($\mathcal{R} = 0.64$) was observed. This ageostrophic peak was due to a drastic drop in V_ψ as the ring center passed over site C2. The ageostrophic flow remained low as the Gulf Stream front shifted south of the site after the ring propagated eastward.

In summary, during both of these events, a cold ring entering the study area gave rise to rapid curvature changes and large horizontal velocity changes in the Gulf Stream. These, in turn, resulted in departures from geostrophy due to substantial contributions of centripetal and tangential accelerations to $\mathbf{V}_a$. Departures from geostrophy, expressed in terms of the ratio $\mathcal{R}$ of the magnitude of ageostrophic current $\mathbf{V}_a$ to that of geostrophic velocity V_ψ, ranged to peaks of 0.2–0.6 during these events.

b. Vertical stretching

Vertical stretching $\partial w/\partial z$ in the upper ocean is estimated using Eq. (18) with baroclinic $\mathbf{V}_\psi$ and ζ_ψ measurements to compute the advection and tendency of vorticity. Advection by the barotropic reference velocity $\mathbf{V}_{3000}$ contributes about 10%–20% to $\partial w/\partial z$, and the contribution by the tendency of barotropic vorticity ζ_{3000} is insignificant. Thus, neglect of $\mathbf{V}_{3000}$ in Eq. (18) adds error only comparable to the uncertainty already in the calculation, $\delta(\partial w/\partial z) \sim 0.02f$ (appendix B).

For illustration, we compute the vertical stretching constituents at the same site, S2, where vorticity estimates were verified in section 5. Figure 12 shows the components, the local tendency $(\partial\zeta_\psi/\partial t)$, and advection $(\mathbf{V}_\psi \cdot \nabla\zeta_\psi)$ of vorticity, together with their sum, the vertical stretching $f(\partial w/\partial z)$. The advection of planetary vorticity is always found to be negligible in these records $(|\mathbf{V}_\psi \cdot \nabla f| \leq |\beta v_{\max}| < 0.25 \times 10^{-10}\ \mathrm{s}^{-2})$. Of the two components, advection of relative vorticity ζ_ψ makes by far the largest contribution to vertical stretching. The tendency term $\partial\zeta_\psi/\partial t$ typically partially cancels the advective changes. However, in most cases the $\partial\zeta_\psi/\partial t$ estimates do not exceed the uncertainty level of 0.6×10^{-10} s^{-2} $(\sim 0.01f^2)$. Thus, with the exception

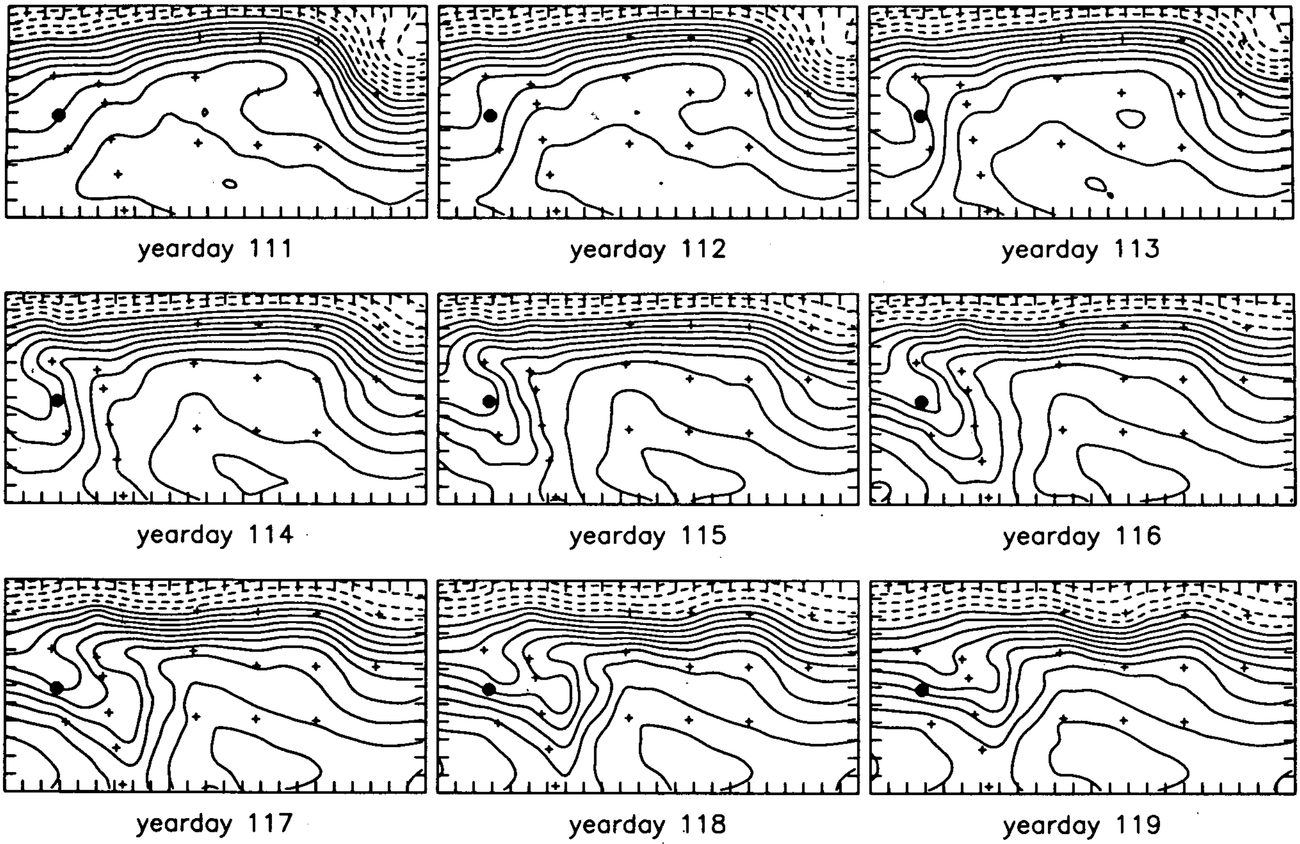

FIG. 11. Objective maps of Z_{12} topography during yeardays 111–119: Z_{12} is contoured at 50-m intervals and depths shallower than 400 m are dashed. The plus marks indicate IES sites and the solid circle indicates site B2.

of a few events, the $\partial\zeta_\psi/\partial t$ contribution at this site is not significant.

Dividing Eq. (18) by $f = 8.56 \times 10^{-5}$ s^{-1}, we obtain estimates of $\partial w/\partial z$ at depth 400 m. Because these calculations all arise from IES maps of Z_{12}, it is appropriate to view $\partial w/\partial z$ as representative of vertical stretching extending through the upper water column. Hence, vertical motion w may be estimated as $w = h(\partial w/\partial z)$ with $h = -400$ m, since $w \approx 0$ at $z = 0$. Positive $\partial w/\partial z$ values signal downwelling or sinking motions (the slope of the vertical velocity profile with height is positive) and, conversely, negative values imply upwelling. Using the values of $f(\partial w/\partial z)$ shown in Fig. 12, we find a mean of $0.01f$ and rms of $0.03f$ for $\partial w/\partial z$ at this site. We estimate the error $\delta(\partial w/\partial z)$ to be about $0.02f$. While this error is substantial, several peaks in vertical stretching with magnitudes as large as $0.12f$ are observed, which greatly exceed the uncertainty level. Next, we will closely examine two of these events, one with large positive $\partial w/\partial z$ values and one with strongly negative values.

Between yeardays 142 and 161, large positive vertical stretching is observed with a maximum $\partial w/\partial z$ of 7.7×10^{-6} s^{-1} ($0.09f$) at yearday 148 (the first arrow on Fig. 12c). The evolution of the Gulf Stream path during a portion of this event is illustrated in Fig. 13. On yearday 142, site S2 is located in a meander trough where the thermocline depth ($Z_{12} \approx 200$ m) is relatively shallow. Subsequently, the thermocline deepens to about 450 m on yearday 152 as a meander crest propagates downstream toward the site. All the other positive $\partial w/\partial z$ peaks (downwelling events) in Fig. 12c also correspond to times when a downstream propagating crest is approaching the site. Thus, we find downwelling in regions downstream of meander crests (which were all propagating downstream).

On the other hand, strong negative $\partial w/\partial z$ is found between yeardays 191 and 196 with peak value of -6.9×10^{-6} s^{-1} ($-0.08f$, arrow at day 193 on Fig. 12c). Examination of the Gulf Stream path during this period (Fig. 13) reveals that site S2 is downstream of a meander trough on yearday 191. Subsequently, the thermocline shoals to about 100 m on yearday 194 as the trough approaches the site. The same pattern is observed for all the strong negative $\partial w/\partial z$ (upwelling) events in Fig. 12c. Hence, upwelling occurs downstream of meander troughs.

These observations at site S2 are in good accord with observations and theory in the atmospheric jet stream (Bluestein 1992), and with RAFOS float and other

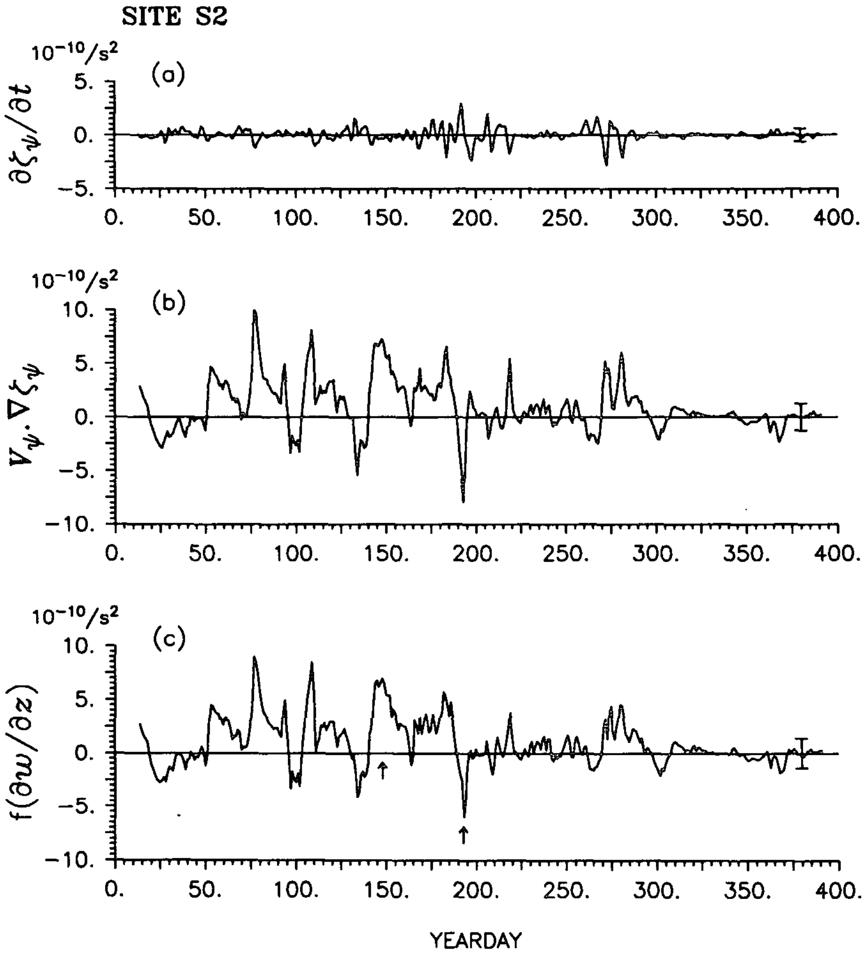

FIG. 12. The quasigeostrophic vorticity equation terms at site S2: (a) local rate of change of ζ_ψ, (b) advective change $\mathbf{V}_\psi \cdot \nabla\zeta_\psi$, and (c) vertical stretching $f(\partial w/\partial z)$. Their units are 10^{-10} s^{-2}. The bars are the expected ±1 std dev uncertainties of each term. The arrows point to extrema on yeardays 148 and 193.

observations in the Gulf Stream reported by Bower and Rossby (1989) and Lindstrom and Watts (1994).

7. Summary

In this work, objectively analyzed maps of thermocline topography (Z_{12}) from IES measurements for one year in the Gulf Stream have been interpreted as maps of the baroclinic, geostrophic streamfunction ψ. To realize and test this interpretation, a constant reduced gravity g^* has been determined to calculate velocities $\mathbf{V}_\psi$ at 400 m relative to 3000 m from the gradient of Z_{12} using Eq. (1). [During work subsequent to completion of this manuscript, He (1993) has shown that g^* can be a function of Z_{12} to achieve an improved empirical and physical representation of the geostrophic currents.]

We have further utilized the Z_{12} maps to calculate the relative vorticity ζ_ψ from $\nabla^2 Z_{12}$ using Eq. (2). We note that the prospects for success might have appeared unlikely for obtaining quantitatively accurate differentiated variables from the Z_{12} maps, because differentiation tends to accentuate measurement noise. However, the success of the effort lays the foundation for applying quasigeostrophic dynamics to daily fields of $\mathbf{V}_\psi(x, y)$ and $\zeta_\psi(x, y)$ in future diagnostic and prognostic studies of Gulf Stream meanders.

Consequently, the goal of this paper has been not only to verify the derived variables, $\mathbf{V}_\psi$ and ζ_ψ, but also to develop a thorough accounting for the errors (appendix A and section 3); $\mathbf{V}_\psi$ was verified against direct current meter measurements at 400 m and 3000 m. The "noise" (rms difference) was about 10 cm s^{-1}, compared to the "signal," which was typically 50–100 cm s^{-1}, and the correlation coefficients were typically 0.94–0.98. The ζ_ψ was verified against a separate method for measuring relative velocity using a rigid-stream model plus path curvature information. The

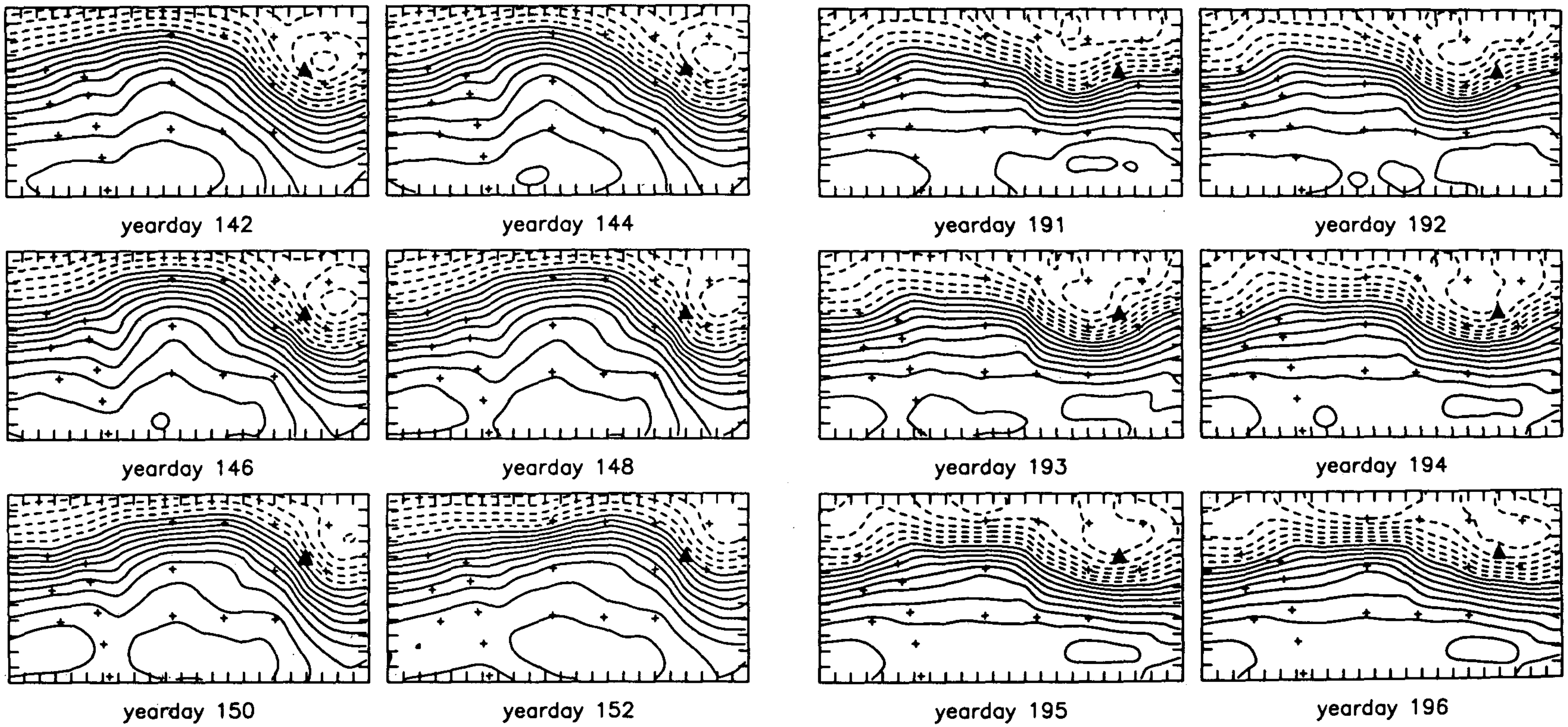

FIG. 13. A sequence of objective analysis maps of Z_{12} (left two columns) at two-day intervals during a positive vertical stretching event (with maximum downwelling) for yeardays 142–152. A solid triangle indicates site S2. (right two columns) Same as left two columns but at daily intervals during a negative vertical stretching event (with maximum upwelling) for yeardays 191–196.

noise (rms difference) was about $0.09f$ compared to the signal, which ranged from $-0.44f$ to $+0.64f$, and the correlation coefficient exceeded 0.86.

The utility of the daily objective ψ maps for the study of quasigeostrophic (QG) dynamics was illustrated by calculations of ageostrophic motion $\mathbf{V}_a$ [Eq. (17)] and vertical stretching $\partial w/\partial z$ [Eq. (18)]. The estimates $\mathbf{V}_a$ were as large as 20 cm s^{-1}, exceeding the estimated uncertainty $\delta(V_a) = 2$–3 cm s^{-1}, with approximately equal contributions from tangential and centripetal accelerations. Note that this QG technique estimates $\mathbf{V}_a$ with considerably less uncertainty than is in $\mathbf{V}_\psi$. We found the ageostrophic departure ratio, $\mathcal{R} = V_a/V_\psi$, to have peak values of 0.2–0.6 during the strong events. Vertical stretching $\partial w/\partial z$ at the 400-m level was estimated by using the quasigeostrophic vorticity equation. Extrema for $\partial w/\partial z$ of $-0.08f$ to $+0.12f$ were primarily due to vorticity advection, exceeding the uncertainty $\delta(\partial w/\partial z) = 0.02f$. Note that this QG technique estimates $\partial w/\partial z$ with far better accuracy at midlatitudes than would result directly from the horizontal divergence $(\partial u/\partial x + \partial v/\partial y)$. Vertical motion estimated with $w = h(\Delta w/\Delta z)$, where depth $h = -400$ m, was similar to the patterns observed in Bower and Rossby (1989) and Lindstrom and Watts (1994). Downwelling (minimum $w \sim -4.4$ mm s^{-1}) occurs downstream of meander crests and upwelling (maximum $w \sim 2.8$ mm s^{-1}) occurs downstream of troughs. We showed in section 6 that, for this set of observations, the barotropic velocity $\mathbf{V}_{3000}$ contributes only about 10%–20% of the leading terms in Eqs. (17) and (18); hence it was neglected.

Overall this work establishes accurate estimates of $\mathbf{V}_\psi$ and ζ_ψ from our objective maps of geostrophic streamfunction generated from IES measurements in the Gulf Stream. Careful error estimates clearly indicate the ability to diagnose quasigeostrophic motions in the development of large meanders.

Acknowledgments. We would like to thank E. Carter for many helpful suggestions and guidance in the early stages of this work, and K. Tracey for her work on the objective analysis mapping of Z_{12}. This study was supported by National Science Foundation Grants OCE85-17746 and OCE87-17144, and the Office of Naval Research Contracts N00014-81-C-0062 and N00014-87-K-1235 at the University of Rhode Island.

APPENDIX A

Derivation of Formulas for Error Covariance $\mathcal{E}$

Here, we derive the error covariance expressions on which all the results using the derivatives of the mapped streamfunction field ($\mathbf{V}_\psi$, ζ_ψ and $\partial V_\psi/\partial t$) are based. We first expand upon the Gauss–Markoff theorem, the fundamental basis of objective analysis.

For a quantity with true value ϕ and objectively estimated value $\hat{\phi}$, the error is defined as $e \equiv \phi - \hat{\phi}$. The expected value of error covariance between two points $(x, y, t)_\alpha$ and $(x', y', t')_\beta$ is

$$\mathcal{E}(x, y, t; x', y', t') \equiv E[e(x, y, t)_\alpha e(x', y', t')_\beta]$$

$$= E[(\phi_\alpha - \hat{\phi}_\alpha)(\phi_\beta - \hat{\phi}_\beta)], \quad (19)$$

where E is a linear, expected value operator. The estimate $\hat{\phi}$ is determined at site α as a linear combination of measurements τ_j, with random noise N_j, at sites $j = 1, \ldots, na$ by

$$\hat{\phi}_\alpha = \sum_{j=1}^{na} W_{\alpha j}(\tau_j + N_j),$$

where $W_{\alpha j}$ are observational weights. Inserting this expression at sites α and β into Eq. (19) and expanding E,

$$\mathcal{E}(x, y, t; x', y', t')$$

$$= E[\phi_\alpha \phi_\beta] - \sum_{j}^{na} W_{\alpha j} E[\phi_\beta \tau_j] - \sum_{l}^{nb} W_{\beta l} E[\phi_\alpha \tau_l]$$

$$+ \sum_{l}^{nb} \sum_{j}^{na} W_{\beta l} W_{\alpha j}(E[\tau_j \tau_l] + \sigma_N^2 \delta_{jl}). \quad (20)$$

In Eq. (20), $E[\phi_\alpha \phi_\beta]$ is the correlation between the true values at $(x, y, t)_\alpha$ and $(x', y', t')_\beta$; $E[\phi_\beta \tau_j]$ is the correlation between the true value at $(x', y', t')_\beta$ and the jth observation contributing to the estimate $\hat{\phi}_\alpha$ at $(x, y, t)_\alpha$; $E[\tau_j \tau_l]$ is the correlation between the jth observation contributing to the estimate $\hat{\phi}_\alpha$ and the lth observation contributing to the estimate $\hat{\phi}_\beta$; σ_N^2 is the noise variance; and δ_{jl} is a Kronecker delta.

In the case $\alpha = \beta$, Eq. (20) yields an error variance at $(x, y, t)_\alpha$,

$$\mathcal{E}(x, y, t; x, y, t)$$

$$= C_{\alpha\alpha} - 2 \sum_{j}^{na} W_{\alpha j} C_{\alpha j} + \sum_{j,i}^{na} W_{\alpha i} W_{\alpha j} C_{ji},$$

where the notations are defined as $C_{\alpha\alpha} \equiv E[\psi_\alpha \psi_\alpha]$, $C_{\alpha j} \equiv E[\psi_\alpha \tau_j]$, and $C_{ji} \equiv E[\tau_j \tau_i] + \sigma^2 \delta_{ji}$.

The minimum error variance is shown by the Gauss–Markoff theorem (Liebelt 1967) to result from

$$W_{\alpha j} = \sum_{i}^{na} C_{\alpha i} C_{ij}^{-1}, \quad (21)$$

for which the error becomes the familiar result,

$$\mathcal{E}(x, y, t; x, y, t) = C_{\alpha\alpha} - \sum_{j,i}^{na} C_{\alpha j} C_{ji}^{-1} C_{\alpha i}, \quad (22)$$

where C_{ji}^{-1} is nonnegative definite.

The error covariance between two optimally interpolated points is found by substituting the optimum weights $W_{\alpha j}$ [Eq. (21)] and $W_{\beta l} = \sum_k^{nb} C_{\beta k} C_{kl}^{-1}$ into Eq. (20):

$$\mathcal{E}(x, y, t; x', y', t') = C_{\alpha\beta} - \sum_{i,j}^{na} C_{\alpha i} C_{ij}^{-1} C_{\beta j} - \sum_{l,k}^{nb} C_{\beta k} C_{kl}^{-1} C_{\alpha l} + \sum_{i,j}^{na} \sum_{l,k}^{nb} C_{\alpha i} C_{ij}^{-1} C_{jl} C_{kl}^{-1} C_{\beta k}. \quad (23)$$

Equations (22) and (23) are the expressions used for calculating the error propagation.

APPENDIX B

Errors in Ageostrophic Velocity and Vertical Stretching Estimates

This appendix presents uncertainty estimates for ageostrophic velocity $\mathbf{V}_a$ in Eq. (17), and for vertical stretching $\partial w/\partial z$ in Eq. (18).

a. Ageostrophic velocity

From Eq. (17), uncertainty $\delta(V_a)$ results from normal and tangential vector components,

$$\delta(V_a) = [\delta^2(V_{an}) + \delta^2(V_{at})]^{1/2}.$$

The respective uncertainties are

$$\delta(V_{an}) = \frac{1}{f}\left[\left(\delta\left(\frac{\partial V_\psi}{\partial t}\right)\right)^2 + \left(\delta(V_\psi)\frac{\partial V_\psi}{\partial s}\right)^2 + \left(V_\psi \delta\left(\frac{\partial V_\psi}{\partial s}\right)\right)^2\right]^{1/2}, \quad (24)$$

and

$$\delta(V_{at}) = \frac{1}{f}[(\delta(\kappa)V_\psi^2)^2 + (2\kappa V_\psi \delta(V_\psi))^2]^{1/2}. \quad (25)$$

They may be determined by substituting relevant values for the variables. The errors $\delta(V_\psi)$ and $\delta(\partial V_\psi/\partial t)$ are typically of order 9.6 cm s^{-1} (section 3a) and 5.9×10^{-5} cm s^{-2} (Kim 1991), respectively; $\delta(\kappa)$ has uncertainty of 10% of the curvature for "normal" cases ($\kappa \leqslant 0.01$ km^{-1}) and 25% of the curvature for "strong" events ($\kappa \geqslant 0.02$ km^{-1}).

The estimate $\partial V_\psi/\partial s$ comes from centered finite differencing ($\partial V_\psi/\partial s \approx \Delta V_\psi/\Delta s$) at spacing $\Delta s = 24$ km, with uncertainty $\delta(\partial V_\psi/\partial s) \approx \sqrt{2}\delta(V_\psi)/2\Delta s \approx 0.28 \times 10^{-5}$ s^{-1}. This may be an overestimate, because it neglects the correlation between V_ψ estimates in a distance Δs.

Combining the above, $\delta(V_{an}) \approx 2.0$ cm s^{-1} [dominated equally by $(1/f)\delta(V_\psi)(\partial V_\psi/\partial s)$ and $(1/f) \times V_\psi \delta(\partial V_\psi/\partial s)$]. For normal cases $\delta(V_{at}) \approx 1.2$ cm s^{-1} and for strong events 2.7 cm s^{-1}. The total error for ageostrophic velocity V_a is then 2.3 cm s^{-1} during relatively straight stream paths and 3.4 cm s^{-1} during high curvature ageostrophic peaks.

b. Vertical motion

The uncertainty in vertical stretching $\partial w/\partial z$ is equivalent to the error in the total estimate of the rhs of Eq. (18) in natural coordinates; that is,

$$\delta\left(\frac{\partial w}{\partial z}\right) = \frac{1}{f}\left[\left(\delta\left(\frac{\partial \zeta_\psi}{\partial t}\right)\right)^2 + \left(\delta(V_\psi)\frac{\partial \zeta_\psi}{\partial s}\right)^2 + \left(V_\psi \delta\left(\frac{\partial \zeta_\psi}{\partial s}\right)\right)^2\right]^{1/2}. \quad (26)$$

Following the above procedures, uncertainties $\delta(\partial\zeta_\psi/\partial t) \approx 0.6 \times 10^{-10}$ s^{-2} and $\delta(\partial\zeta_\psi/\partial s) \approx 0.2 \times 10^{-11}$ cm^{-1} s^{-1} are obtained respectively for the separations $\Delta t = 24$ h and $\Delta s = 28$ km, and $\delta(\zeta_\psi) = 0.76 \times 10^{-5}$ s^{-1} (from section 3b).

We also substituted into Eq. (26) typical values of $\partial\zeta_\psi/\partial s = 0.8 \times 10^{-11}$ cm^{-1} s^{-1}, $\delta(V_\psi) = 9.6$ cm s^{-1}, $V_\psi = 70$ cm s^{-1}, and $f = 8.56 \times 10^{-5}$ s^{-1}. Altogether, we estimate the error in vertical stretching $\delta(\partial w/\partial z) = 1.7 \times 10^{-6}$ s^{-1}, which is $0.02f$.

REFERENCES

Ames, W. F., 1977: *Numerical Methods for Partial Differential Equations.* Academic Press, 365 pp.

Bane, J. M., L. M. O'Keefe, R. S. Ault, and D. R. Watts, 1989: The Gulf Stream dynamics; current meter data report, January 1984 to January 1985. Tech. Rep. CMS 89-1, Marine Science Program, University of North Carolina–Chapel Hill, 253 pp.

Bluestein, H. B., 1992: *Synoptic-Dynamic Meteorology in Midlatitudes,* Vol. 1. Oxford University Press, 431 pp.

Bower, A. S., and T. Rossby, 1989: Evidence of cross-frontal exchange processes in the Gulf Stream based on isopycnal RAFOS floats data. *J. Phys. Oceanogr.,* **19,** 1177–1190.

Bretherton, F. P., R. E. Davis, and C. B. Fandry, 1976: A technique for objective analysis and design of oceanographic experiments applied to MODE-73. *Deep-Sea Res.,* **23,** 559–582.

Bryden, H. L., and N. P. Fofonoff, 1977: Horizontal divergence and vorticity estimates from velocity and temperature measurements in the MODE region. *J. Phys. Oceanogr.,* **7,** 329–337.

Halkin, D., and T. Rossby, 1985: The structure and transport of the Gulf Stream at 73°W. *J. Phys. Oceanogr.,* **15,** 1439–1452.

He, Y., 1993: Determining the baroclinic geostrophic velocity structure with inverted echo sounders. M.S. thesis, Graduate School of Oceanography, University of Rhode Island, Narragansett, 135 pp.

Holton, J. R., 1979: *An Introduction to Dynamic Meteorology.* Academic Press, 391 pp.

Inoue, H., 1986: A least-squares smooth fitting for irregularly spaced data: Finite-element approach using the cubic B-spline basis. *Geophysics,* **51,** 2051–2066.

Johns, E., D. R. Watts, and H. T. Rossby, 1989: A test of geostrophy in the Gulf Stream. *J. Geophys. Res.,* **94,** 3211–3222.

Johns, W. E., T. J. Shay, J. M. Bane, and D. R. Watts, 1994: Gulf Stream structure, transport, and recirculation near 68°W. *J. Geophys. Res.,* in press.

Kim, H.-S., 1991: An observational streamfunction in the Gulf Stream. M.S. thesis, Graduate School of Oceanography, University of Rhode Island, Narragansett, 126 pp.

——, 1994: An equivalent-barotropic data-assimilating model of Gulf Stream meanders. Ph.D. thesis, Graduate School of Oceanography, University of Rhode Island, Narragansett, 95 pp.

Liebelt, P. B., 1967: *An Introduction to Optimal Estimation.* Addison-Wesley, 273 pp.

Lindstrom, S. S., and D. R. Watts, 1994: Vertical motion in the Gulf Stream near 68°W, *J. Phys. Oceanogr.,* **24,** 2321–2333.

Pond, S., and G. L. Pickard, 1983: *Introductory Dynamical Oceanography.* Pergamon, 329 pp.

Qian, X., and D. R. Watts, 1992: The SYNOP experiment: Bottom pressure maps for the Central Array May 1988 to August 1990. Tech. Rep. 92-3, Graduate School of Oceanography, University of Rhode Island, Narragansett, 187 pp.

Tracey, K. L., and D. R. Watts, 1986: The Gulf Stream dynamics experiment: Inverted echo sounder data report for the April 1983 to June 1984 deployment period. Tech. Rep. 86-4, Graduate School of Oceanography, University of Rhode Island, Narragansett, 228 pp.

——, M. Cronin, and D. R. Watts, 1985: The Gulf Stream dynamics experiment: Inverted echo sounder data report for the June 1984 to May 1985 deployment period. Tech. Rep. 85-3, Graduate School of Oceanography, University of Rhode Island, Narragansett, 176 pp.

Watts, D. R., and T. Rossby, 1977: Measuring dynamic heights with Inverted Echo Sounders: Results from MODE. *J. Phys. Oceanogr.,* **7,** 345–358.

——, K. L. Tracey, and A. I. Friedlander, 1989: Producing accurate maps of the Gulf Stream thermal front using objective analysis. *J. Geophys. Res.,* **94,** 8040–8052.